American Mineralogist, Volume 94, pages 181–189, 2009

Crystal chemistry of the magnetite-ulvöspinel series

Ferdinando Bosi,[1,2,*] Ulf Hålenius,[1] and Henrik Skogby[1]

[1]Department of Mineralogy, Swedish Museum of Natural History, Box 50007, 10405 Stockholm, Sweden
[2]Dipartimento di Scienze della Terra, Sapienza Università di Roma, P.le A. Moro, 5, I-00185 Rome, Italy

Abstract

Spinel single crystals of 19 compositions along the magnetite-ulvöspinel join were synthesized by use of a flux-growth method. To obtain quantitative site populations, the crystals were analyzed by single-crystal X-ray diffraction, electron-microprobe techniques, and Mössbauer spectroscopy. All results were processed by using an optimization model.

The unit-cell parameter, oxygen fractional coordinate, and tetrahedral bond length increase with increasing ulvöspinel component, whereas the octahedral bond length decreases marginally. These changes result in sigmoidal crystal-chemical relationships consistent with cation substitutions in fully occupied sites. As a first approximation, the Akimoto model $^{T}(Fe^{3+}_{1-X}Fe^{2+}_{X})^{M}(Fe^{2+}Fe^{3+}_{1-X}Ti_{X})O_4$ describes the cation substitutions. Deviations from this model can be explained by an electron exchange reaction $^{T}Fe^{2+} + {}^{M}Fe^{3+} = {}^{T}Fe^{3+} + {}^{M}Fe^{2+}$, which causes $^{M}Fe^{2+} \neq 1$ and $^{T}Fe^{2+}/Ti \neq 1$. The resultant S-shaped trends may be related to a directional change in the electron exchange reaction at Ti ≈ 0.7 apfu. In general, variations in structural parameters over the whole compositional range can be split into two contributions: (1) a linear variation due to the $^{T}Fe^{3+} + {}^{M}Fe^{3+} = {}^{T}Fe^{2+} + {}^{M}Ti^{4+}$ chemical substitution and (2) non-linear variations caused by the internal electron exchange reaction.

In accordance with bond-valence theory, strained bonds ascribable to steric effects characterize the structure of magnetite-ulvöspinel crystals. To relax the bonds and thereby minimize the internal strain under retained spinel space group symmetry, the electron exchange reaction occurs.

Keywords: Spinel, Mössbauer spectroscopy, crystal synthesis, crystal structure

Introduction

Multiple oxides with spinel-type structure are common accessory minerals in a wide range of geological environments, from the upper mantle to the crust. Due to their magnetic properties, they are of interest in geophysical and technological research. Oxide spinels have the general formula of AB_2O_4, where the A and B refer to cations of either 2+ and 3+ valence ($A^{2+}B^{3+}_2O_4$, so-called 2-3 spinels) or of 4+ and 2+ valence ($A^{4+}B^{2+}_2O_4$, so-called 4-2 spinels). The structure is generally described as a slightly distorted cubic close packed (CCP) array of anions, in which the A and B cations are distributed in one-eighth of all tetrahedral (T) and half of all octahedral (M) sites. This cation occupancy leads to two different ordered cation distribution schemes. The normal spinel, where the A cation occupies the T site and the two B cations occupy the M sites; and the inverse spinel, where one of the B cations occupies the T site and the remaining A and B cations occupy the M sites.

The unit cell is face-centered cubic (space group $Fd\bar{3}m$) and it contains 32 anions. The cations are fixed at special positions 8*a* (T) and 16*d* (M), as well as the anions (32*e*). However, the latter have a variable fractional coordinate (*u*,*u*,*u*). The *u*-parameter is related to the distortion of the CCP array: for the ideal close-packed structure, $u = 0.25$. A distortion of the CCP arises when $u \neq 0.25$. The structure of spinel can be described by using the unit-cell parameter *a* and oxygen fractional coordinate *u* (e.g., Lavina et al. 2002).

Ideal magnetite (Fe_3O_4) and ulvöspinel (Fe_2TiO_4) have a cubic inverse spinel structure, with the structural formulae $^{T}(Fe^{3+})^{M}(Fe^{2+}Fe^{3+})O_4$ and $^{T}(Fe^{2+})^{M}(Fe^{2+}Ti^{4+})O_4$, respectively. They represent important minerals in nature because they are essential carriers of the remanent magnetism in rocks. Complete solid solution between magnetite and ulvöspinel exists at temperatures above 600 °C (Price 1981). The intermediate compositions, known as titanomagnetite ($Fe^{2+}_{1+X}Fe^{3+}_{2-2X}Ti_XO_4$), are formed by the replacement of two Fe^{3+} cations by Fe^{2+} and Ti^{4+}. The ordering of these cations over T and M sites is still uncertain. Although some studies have indicated that Ti^{4+} might exist in the tetrahedral sites (e.g., Stout and Bayliss 1980; Sedler et al. 1994), other studies have suggested that Ti^{4+} is always limited to the octahedral sites (e.g., Fujino 1974; Wechsler et al. 1984). Basically three models, based largely upon magnetic considerations, have been proposed to describe the ordering of Fe^{2+}, Fe^{3+}, and Ti^{4+} in titanomagnetite:

Akimoto (1954)
$^{T}(Fe^{3+}_{1-X}Fe^{2+}_{X})^{M}(Fe^{2+}Fe^{3+}_{1-X}Ti_{X})O_4$ for $0 \leq X \leq 1.0$ (1)

Néel (1955) and Chevallier et al. (1955)
$^{T}(Fe^{3+})^{M}(Fe^{2+}_{1+X}Fe^{3+}_{1-2X}Ti_{X})O_4$ for $0 \leq X \leq 0.5$, and
$^{T}(Fe^{3+}_{2-2X}Fe^{2+}_{2X-1})^{M}(Fe^{2+}_{2-X}Ti_{X})O_4$ for $0.5 \leq X \leq 1.0$ (2)

O'Reilly and Banerjee (1965)
$^{T}(Fe^{3+})^{M}(Fe^{2+}_{1+X}Fe^{3+}_{1-2X}Ti_{X})O_4$ for $0 \leq X \leq 0.2$,
$^{T}(Fe^{3+}_{1.2-X}Fe^{2+}_{X-0.2})^{M}(Fe^{2+}_{1.2}Fe^{3+}_{0.8-X}Ti_{X})O_4$ for $0.2 \leq X \leq 0.8$,
and $^{T}(Fe^{3+}_{2-2X}Fe^{2+}_{2X-1})^{M}(Fe^{2+}_{2-X}Ti_{X})O_4$ for $0.8 \leq X \leq 1$. (3)

* E-mail: ferdinando.bosi@uniroma1.it

Stephenson (1969) and Bleil (1971, 1976), however, suggested that the distribution of Fe^{2+} and Fe^{3+} over the T and M sites change as a function of temperature. They indicated that at high temperature (about 1300 °C), the cation distribution approaches the Akimoto model, whereas at low temperature it follows the Néel model. By contrast, the results of O'Donovan and O'Reilly (1980) and Wechsler et al. (1984) did not support temperature-dependent cation distribution in titanomagnetites. Some studies (e.g., Wechsler et al. 1984; Senderov et al. 1993) have suggested the presence of cation vacancies (non-stoichiometry) in titanomagnetite. The non-stoichiometry is supposed to cause non-linear S-shaped (concavo-convex) variations in the crystal-chemical relationships, e.g., on a plot of the *a*-parameter vs. ulvöspinel content.

In the present study, which is a continuation of the work presented in Bosi et al. (2008), a multi-analytical approach was used to characterize synthetic single crystals on the $FeFe_2O_4$-Fe_2TiO_4 join. As most of the magnetic, electrical, and thermochemical properties of titanomagnetites are very closely related to their cation distribution, the aim of the study was to quantitatively detail the site-occupancy to explore the interplay between chemical composition and structural arrangement.

Experimental methods

Synthesis

Spinel crystals having compositions along the $FeFe_2O_4$-Fe_2TiO_4 solid-solution join were synthesized by a flux-growth method. The samples were grown from saturated melts under slow cooling from 1200 to 900 °C. To control the oxygen fugacity, a continuous flow of CO_2 and H_2 was passed through the furnace tube. Details of the synthesis procedures for samples FeTib1–4, grown using a flux mixture of BaO and B_2O_3, are described in Bosi et al. (2008). The other samples were grown using an $Na_2B_4O_7$ flux under an oxygen fugacity ranging from 10^{-8} to 10^{-14} bars, largely in response to the temperature variation during cooling. Successful synthesis products contained spinel crystals with sizes ranging up to 4 mm. In addition, borate crystals and, in a few cases, ilmenite, rutile, metallic iron, and a Ba-Fe-Ti-O compound were also present.

Single-crystal structural refinement (SREF)

Nineteen synthetic single crystals (Ø ≈ 130 μm) were used in the present study. Each was mounted on a Siemens P4 automated four-circle, single-crystal diffractometer. Unit-cell parameters were measured by centering 52 reflections (13 independent and their Friedel pairs, on both sides of the direct beam) in the range 85–95 °2θ, with Mo$K\alpha_1$ radiation (0.70930 Å). Intensity data were collected at a temperature of 296 K using Mo$K\alpha$ radiation (0.71073 Å) monochromatized by a flat graphite crystal in the 3–95 °2θ range with the ω-scan method. For collection of diffraction intensity data, one-eighth of the reciprocal space was examined with the ω scan method at a fixed scan range (2.4°). The scan speed was variable (1.5–14.6 °/min), depending on reflection intensity, as estimated through pre-scans. The background was measured with a stationary counter and crystal at the beginning and end of each scan, in both cases for half the scan time. Three standard reflections were monitored every 47 measurements.

Data reduction was performed with the SHELXTL-PC program package. Intensities were corrected for polarization and Lorentz effects. Absorption correction was accomplished with a semi-empirical method (North et al. 1968). Structural refinement was carried out with the SHELXL-97 program (Sheldrick 1997). All reflections were used in the refinement. No significant deviations from $Fd\bar{3}m$ symmetry were noted. Appearance of forbidden space-group reflections such as 200 were attributed, on the basis of ψ-scan checks, to double reflection. Variable parameters during the structural refinement were overall scale factor, oxygen coordinate, site-scattering values, atomic displacement parameters, and extinction parameter. Setting the origin at $\bar{3}m$, initial atomic positions for the oxygen atom were taken from the structure of spinel (Bosi et al. 2007). No chemical constraints were applied during the refinement. The T site was modeled with an Fe scattering factor and with a fixed occupancy of 1.000, because refinement with unconstrained T-occupancy showed no significant deviations. The occupancy of the M site was refined and modeled considering the presence of Fe, because this led to the best agreement factors based on an F^2 test. For the magnetite, the M-site occupancy was freely refined to a value of 1.003(4) and, then fixed to unity for the final refinement. Three isotropic, full-matrix refinement cycles were followed by anisotropic cycles until convergence was attained. The shifts in all refined parameters were less than their estimated standard deviation. Table 1 summarizes unit-cell parameter, oxygen fractional coordinate, bond lengths, site occupancy (expressed as mean atomic number), displacement parameters, and refinement details.

Electron microprobe analysis (EMPA)

Electron-microprobe analyses were carried out on the same crystals used for the XRD refinements. The analyses were obtained by WDS methods, using a Cameca SX50 instrument at the University of Uppsala operating at an accelerating potential of 20 kV and a sample current of 15 nA. Standards were synthetic $MnTiO_3$ (for Ti) and Fe_2O_3 (for Fe). Al_2O_3 was checked for, using a corundum standard, as a possible contaminant from the furnace tube. Sodium and Ba contamination from the flux was not detected. For raw data reduction, the PAP matrix correction procedure was applied (Pouchou and Pichoir 1991). The results, which are summarized in Table 2, represent mean values of a minimum of 10 spot analyses per analyzed crystal and their standard errors (below 1%) demonstrate that the crystals are homogeneous.

Mössbauer spectroscopy (MS)

With the purpose of determining $Fe^{3+}/\Sigma Fe$-ratios and the Fe-site distribution in the magnetite end-member, ^{57}Fe Mössbauer spectra were obtained on absorbers prepared by placing finely ground crystals between plastic foils in a ca. 2.5 mm circular aperture of a Pb-disk. Spectra were collected at room temperature using a conventional spectrometer system operated in constant acceleration mode with a nominal 10 mCi ^{57}Co/Rh point source. Spectral data were recorded for the velocity range –10 to +10 mm/s in a multichannel analyzer using 1024 channels. After velocity calibration against room temperature α-iron foil spectra, raw spectral data were folded and fitted using a least-square fitting program (Jernberg and Sundqvist 1983). Lorentzian lines, equal recoil-free fractions, and equal intensity of the quadrupole components were assumed in the fitting procedure. For the magnetic spectra, the intensity ratios among the individual lines were constrained to a 3:2:1 relationship. Experimental procedure and results for the high-Ti solid-solution members have been reported in detail in Bosi et al. (2008).

Results and discussion

Chemical and Mössbauer data

The work by Bosi et al. (2008) showed that their samples of Ti-rich solid-solution members were stoichiometric. Provided that the synthesized end-member magnetite is also stoichiometric, we can assume that the remaining Fe-rich compositions along this binary are stoichiometric. On this basis, the $Fe^{3+}/\Sigma Fe$ ratios and atomic proportions were calculated assuming charge balance and stoichiometry (Table 2). The stoichiometry of samples is also well supported by the match between number of electrons per formula unit derived from EMPA and SREF data (Table 2). Consequently, the compositional changes along this magnetite-ulvöspinel solid solution are described by the classic substitution $2Fe^{3+} \leftrightarrow Fe^{2+} + Ti^{4+}$.

The analysis of the magnetite Mössbauer spectra resulted in hyperfine parameters for Fe species in tetrahedral and octahedral sites virtually identical to those reported in literature (e.g., Häggström et al. 1978). From the relative peak areas of the three sextets fitted to the spectra, the calculated $Fe^{3+}/\Sigma Fe$ ratio is 0.68(2). This value is consistent with the chemical composition of the ideal end-member magnetite: $Fe^{2+} = 1.00(1)$ and $Fe^{3+} = 2.00(1)$ atoms per formula unit (apfu). The spectrum also indicates that the structural environment of Fe^{2+} is octahedral, whereas that of Fe^{3+} is both octahedral and tetrahedral. The resulting cation distribution for the present magnetite is in excellent agreement with the ideal structural formula $^{T}(Fe^{3+})$

TABLE 1. Structural parameters and refinement details

Crystal	Mgt100	FeTi10C	FeTi50B	FeTi10Ai	FeTi10Ao	FeTi20A	FeTi30A	FeTi50Bd	FeTi50C
a	8.3967(3)	8.4067(5)	8.4095(5)	8.4145(5)	8.4250(5)	8.4348(5)	8.4569(4)	8.4716(4)	8.4875(4)
u	0.25476(10)	0.25496(10)	0.25502(8)	0.25502(9)	0.25535(11)	0.25596(11)	0.25660(10)	0.25797(11)	0.25827(10)
T-O	1.8872(15)	1.8923(15)	1.8938(12)	1.8950(14)	1.9021(16)	1.9133(16)	1.9276(15)	1.9511(116)	1.9592(15)
M-O	2.0600(8)	2.0608(8)	2.0610(7)	2.0622(8)	2.0622(9)	2.0597(9)	2.0599(8)	2.0526(9)	2.0541(8)
T-m.a.n.	26	26	26	26	26	26	26	26	26
M-m.a.n.	26	25.66(8)	25.62(7)	25.63(9)	25.70(8)	25.06(10)	24.86(10)	24.42(8)	24.45(6)
U_{11} (O)	0.0072(2)	0.0069(2)	0.0078(1)	0.0057(2)	0.0115(3)	0.0073(2)	0.0087(2)	0.0109(3)	0.0128(3)
U_{23} (O)	–0.0005(3)	–0.0008(2)	–0.0007(2)	–0.0006(2)	–0.0007(3)	–0.0006(3)	–0.0004(2)	–0.0007(2)	–0.0006(3)
U_{11} (T)	0.0056(1)	0.00506(9)	0.0059(1)	0.0038(12)	0.0092(2)	0.0045(1)	0.0059(1)	0.0076(1)	0.0098(2)
U_{11} (M)	0.0071(1)	0.00663(7)	0.00735(7)	0.00534(9)	0.0107(1)	0.0050(1)	0.00591(9)	0.0067(1)	0.0088(2)
U_{23} (M)	0.00072(7)	0.00100(7)	0.00092(6)	0.00103(7)	0.00092(8)	0.00068(7)	0.00043(6)	–0.00003(6)	–0.00011(7)
EXTI	0.095(4)	0.0059(4)	0.0046(5)	0.016(1)	0.0064(9)	0.010(1)	0.018(1)	0.019(1)	0.024(1)
Reflections	703	706	706	706	706	706	715	727	727
Refl. unique	164	165	165	165	165	165	167	169	169
*R*1, $I > 2\sigma(I)$	1.97	1.47	1.85	2.14	2.37	2.21	1.90	2.03	1.85
w*R*2	4.48	2.68	3.59	4.13	5.90	4.54	4.00	4.79	4.22
GooF	1.232	1.120	1.253	1.369	1.183	1.320	1.288	1.174	1.066

Crystal	FeTi40A	FeTi60A	FeTi70A	FeTi80Ac	FeTi80Af	FeTib3	FeTib2	FeTib4	FeTib1c	FeTib1b
a	8.4972(5)	8.4975(4)	8.5052(5)	8.5059(5)	8.5079(4)	8.5139(5)	8.5220(4)	8.5274(5)	8.5307(4)	8.5322(4)
u	0.25855(12)	0.25917(15)	0.25947(16)	0.25924(10)	0.25912(12)	0.25980(11)	0.26025(10)	0.26065(12)	0.26077(10)	0.26074(13)
T-O	1.9655(18)	1.9747(22)	1.9810(24)	1.9777(15)	1.9764(17)	1.9878(16)	1.9964(15)	2.0035(18)	2.0061(15)	2.0060(19)
M-O	2.0542(10)	2.0494(12)	2.0489(13)	2.0509(8)	2.0523(9)	2.0484(9)	2.0469(8)	2.0451(9)	2.0449(8)	2.0455(10)
T-m.a.n.	26	26	26	26	26	26	26	26	26	26
M-m.a.n.	24.27(9)	24.36(12)	24.58(13)	24.13(8)	24.22(8)	24.08(9)	24.06(9)	24.06(12)	23.83(9)	23.63(12)
U_{11} (O)	0.0128(3)	0.0108(3)	0.0165(4)	0.0111(3)	0.0113(3)	0.0113(3)	0.0110(3)	0.0156(3)	0.0119(3)	0.0143(4)
U_{23} (O)	–0.0011(2)	–0.0019(3)	–0.0011(3)	–0.0016(2)	–0.0019(2)	–0.0024(2)	–0.0029(2)	–0.0034(2)	–0.0038(2)	–0.0035(8)
U_{11} (T)	0.0093(2)	0.0073(2)	0.0130(2)	0.0075(1)	0.0075(1)	0.0075(1)	0.0073(2)	0.0117(1)	0.0077(2)	0.0104(2)
U_{11} (M)	0.0077(1)	0.0058(1)	0.0115(2)	0.0057(1)	0.0057(1)	0.0054(1)	0.0049(1)	0.0092(1)	0.0051(1)	0.0076(2)
U_{23} (M)	–0.00020(6)	–0.00027(8)	–0.00049(7)	–0.00025(5)	–0.00022(6)	–0.00051(5)	–0.00058(4)	–0.00068(5)	–0.00068(5)	–0.00071(6)
EXTI	0.017(2)	0.0078(9)	0.012(2)	0.045(3)	0.035(2)	0.020(2)	0.014(2)	0.011(1)	0.038(3)	0.067(5)
Reflections	727	727	721	827	727	715	733	733	733	733
Refl. unique	169	169	169	169	169	170	170	179	170	170
*R*1, $I > 2\sigma(I)$	2.81	2.51	2.79	1.81	1.87	2.08	2.77	2.81	1.98	2.57
w*R*2	5.87	5.65	7.86	4.32	4.30	4.96	5.28	6.13	5.25	6.48
GooF	1.170	1.251	1.147	1.157	1.221	1.290	1.238	1.410	1.320	1.322

Notes: *a* = unit-cell parameter (Å); *u* = oxygen fractional coordinate; T-O and M-O = tetrahedral and octahedral bond lengths (Å), respectively; T- and M-m.a.n. = T- and M-mean atomic number; *U* = displacement parameter (Å^2); $U_{11} = U_{22} = U_{33}$ and $U_{12} = U_{13} = U_{23}$ (=0 for the T site due to symmetry reasons); EXTI = extinction parameter; *R*1 (%) and *wR*2 (%) = agreement indexes (Sheldrick 1997); GooF = goodness of fit. Space group $Fd\bar{3}m$. Origin fixed at $\bar{3}m$. $Z = 8$. Reciprocal space range: $0 \le h \le 17$; $0 \le k \le 17$; $0 \le l \le 17$.

$^{M}(Fe^{3+}Fe^{2+})O_4$. Because of the rapid electron exchange (electron delocalization) between Fe^{2+} and Fe^{3+} at the M sites, a dynamic electronic disorder occurs. As an equal number of $^{M}Fe^{2+}$ and $^{M}Fe^{3+}$ share an electron, an average valence state of 2.5 can be assumed for ^{M}Fe.

Crystal structure

Structural data show that a strict correlation exists between the unit-cell parameter and *u*-parameter (Fig. 1). The latter varies from 0.2548 (magnetite) to 0.2607 (ulvöspinel), indicating a displacement of oxygen along the direction [111]. This displacement causes an increase in the CCP distortion, which results in a larger T-O at the expense of a smaller M-O. The reduction of M-O length is in fact a consequence of the increase in *u* parameter, by which the lengths of two non-equivalent octahedral edge—one shared ($^{M}O\text{-}O_{sh}$) with adjacent M sites and the other unshared ($^{M}O\text{-}O_{unsh}$)—are determined. As the shortening of $^{M}O\text{-}O_{sh}$ (from 2.86 to 2.76 Å) is greater than the lengthening of $^{M}O\text{-}O_{unsh}$ (from 2.97 to 3.02 Å), M-O lengths decrease with increasing Ti content. Bond lengths and *a*-parameter relationships (Fig. 2) are characterized by a strong T-O increase (from 1.887 to 2.006 Å) with increasing *a*-parameter, whereas the M-O lengths decrease only slightly (from 2.060 to 2.045 Å). Hence, the structural variations along the entire magnetite-ulvöspinel join are mainly driven by changes in T-O rather than M-O bond length. In particular, the CCP distortion is closely related to the T-O variations, which greatly affects variations in $^{M}O\text{-}O_{sh}$ (Fig. 3).

As the size of the Ti^{4+} cation is smaller than those of Fe^{3+} and Fe^{2+} (Shannon 1976), the observed increase in T-O with increasing ulvöspinel-component reflects $^{T}Fe^{3+}$ replacement by $^{T}Fe^{2+}$ rather than by $^{T}Ti^{4+}$. This finding is also consistent with the unchanged T-site scattering factor observed during the structural refinements. Moreover, the decrease in M-site scattering factors (Table 1) agrees with an introduction of Ti into the M site. The negative correlation between T-O and M-site scattering (r^2 = 0.94) supports the conclusion that Fe^{2+} and Ti^{4+} are introduced into T and M sites, respectively.

Cation distribution and bond valence

Structural refinement analysis showed that the Ti^{4+} cation occupies exclusively the M site. Consequently, the intracrystalline Fe^{2+} and Fe^{3+} distribution over the T and M sites was estimated by

Table 2. Chemical composition by EMPA

Crystal	Mgt100*	FeTi10C	FeTi50B	FeTi10Ai	FeTi10Ao	FeTi20A	FeTi30A	FeTi50Bd	FeTi50C
TiO_2 (wt%)	–	3.17(18)	3.30(17)	6.44(19)	8.43(20)	12.35(17)	16.10(10)	20.14(11)	22.55(16)
FeO_{tot}	92.66(77)	86.37(99)	87.39(87)	87.56(36)	86.29(51)	82.09(34)	79.55(30)	73.83(96)	74.17(32)
Al_2O_3	–	–	–	–	–	0.66(6)	–	0.61(8)	–
FeO†	30.89	32.59	33.08	36.91	38.87	42.48	45.82	49.05	51.77
Fe_2O_3†	68.65	59.76	60.36	56.29	52.70	44.02	37.49	27.54	24.89
Total	99.54	95.53	96.74	99.64	100.00	99.51	99.40	97.34	99.22
Ti^{4+} (apfu)	–	0.096(7)	0.098(7)	0.186(6)	0.242(7)	0.354(5)	0.462(3)	0.586(8)	0.644(5)
Fe^{2+}	1.000(11)	1.096(14)	1.098(13)	1.186(8)	1.242(9)	1.354(7)	1.462(3)	1.586(6)	1.644(5)
Fe^{3+}	2.000(7)	1.808(13)	1.803(12)	1.628(10)	1.515(11)	1.263(9)	1.076(5)	0.801(12)	0.711(7)
Al^{3+}	–	–	–	–	–	0.030(4)	–	0.028(4)	–
Total	3.000	3.000	3.000	3.000	3.000	3.000	3.000	3.000	3.000
e^-_{EMPA} (epfu)	78	77.6(5)	77.6(5)	77.3(4)	77.0(4)	76.2(3)	76.1(2)	75.3(4)	75.4(3)
e^-_{SREF}	78	77.3(2)	77.3(1)	77.3(2)	77.4(2)	76.1(2)	75.7(2)	74.8(2)	74.9(1)
Δe^-	0	0.3(5)	0.3(5)	0.0(4)	0.4(4)	0.1(4)	0.4(3)	0.4(4)	0.5(3)

Crystal	FeTi40A	FeTi60A	FeTi70A	FeTi80Ac*	FeTi80Af*	FeTib3*	FeTib2*	FeTib4*	FeTib1c*	FeTib1b*
TiO_2 (wt%)	25.15(16)	24.30(21)	26.55(32)	26.57(15)	26.69(11)	28.10(19)	29.69(33)	31.88(21)	32.79(37)	33.45(32)
FeO_{tot}	72.61(20)	73.10(53)	71.41(42)	71.53(21)	71.32(22)	69.46(55)	68.10(40)	66.07(38)	65.64(28)	65.43(31)
Al_2O_3	–	–	–	–	–	–	–	–	–	–
FeO†	54.37	53.51	55.64	55.71	55.78	56.86	58.30	60.25	61.21	61.93
Fe_2O_3†	20.27	21.78	17.52	17.59	17.27	14.01	10.89	6.46	4.93	3.89
Total	99.79	99.58	99.71	99.87	99.73	98.97	98.88	98.59	98.93	99.27
Ti^{4+} (apfu)	0.713(4)	0.690(7)	0.752(8)	0.751(4)	0.755(3)	0.800(7)	0.845(8)	0.908(6)	0.930(8)	0.945(7)
Fe^{2+}	1.713(4)	1.690(6)	1.752(8)	1.751(4)	1.755(3)	1.800(6)	1.845(8)	1.908(6)	1.930(8)	1.945(7)
Fe^{3+}	0.575(6)	0.619(10)	0.496(12)	0.497(6)	0.489(5)	0.399(10)	0.310(12)	0.184(9)	0.140(12)	0.110(11)
Al^{3+}	–	–	–	–	–	–	–	–	–	–
Total	3.000	3.000	3.000	3.000	3.000	3.000	3.000	3.000	3.000	3.000
e^-_{EMPA} (epfu)	75.1(2)	75.2(3)	75.0(4)	75.0(2)	75.0(2)	74.8(3)	74.6(4)	74.4(3)	74.3(4)	74.2(4)
e^-_{SREF}	74.6(2)	74.7(2)	75.2(3)	74.3(2)	74.5(2)	74.2(2)	74.1(1)	74.1(2)	73.7(2)	73.3(3)
Δe^-	0.5(3)	0.5(4)	0.2(5)	0.7(3)	0.5(3)	0.6(4)	0.5(4)	0.3(4)	0.6(5)	0.9(5)

Notes: Cations on the basis of 4 O atoms per formula unit (apfu). Digits in parentheses are estimated uncertainties (1σ): for reported oxide concentrations, they represent standard deviations of several analyses on individual crystals, whereas, for cations, they were calculated according to Wood and Virgo (1989). e^-_{EMPA} and e^-_{SREF} = number of electrons per formula unit (epfu) derived from EMPA and SREF. Δe^- = absolute deviation between e^-_{EMPA} and e^-_{SREF}.
* $Fe^{2+}/\Sigma Fe$ ratio obtained from MS (see text for magnetite, and Bosi et al. 2008 for the other crystals) is consistent with stoichiometry.
† From stoichiometry.

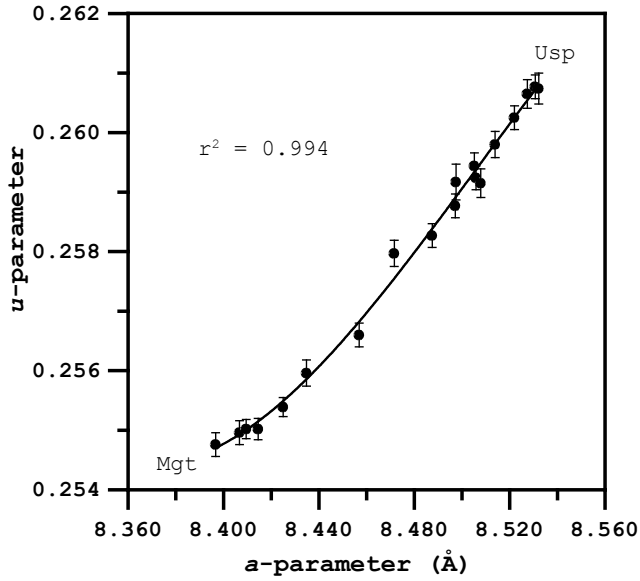

Figure 1. Plot of the unit-cell parameter (*a*) and oxygen fractional coordinate (*u*) showing the strong correlation between these structural parameters. Solid line represents a non-linear regression. Symbol dimensions and error bars, where shown, are proportional to 2σ.

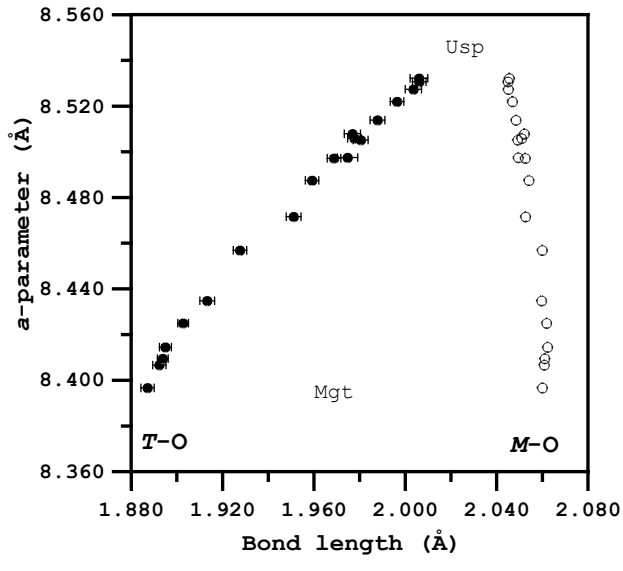

Figure 2. The relationships between *a*-parameter and bond lengths T-O and M-O show that the structure variations are strongly affected by T-O. Symbol dimensions and error bars, where shown, are proportional to 2σ.

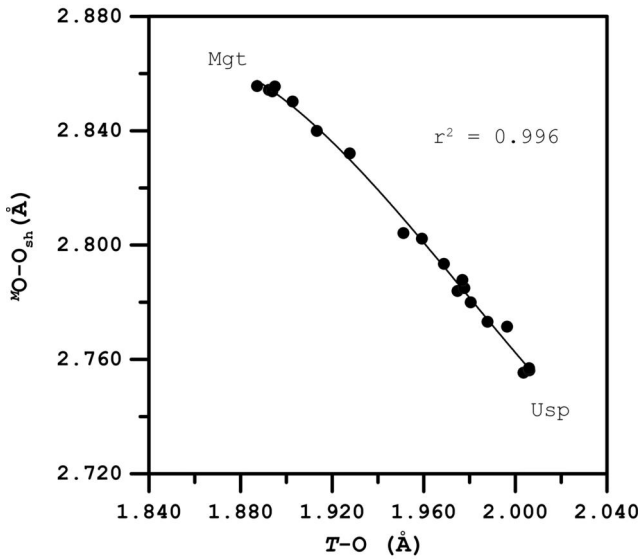

FIGURE 3. Variation in ^{M}O-O$_{sh}$ share edge vs. T-O is better described by a non-linear fitting. Variations relative to ^{M}O-O$_{sh}$ are linked to the octahedron and CCP distortion. Error bars are proportional to 2σ.

an optimization program applying a minimization function, F(X_i), to the calculated and observed residuals, derived from structural (T-O, M-O, *u*, *a*) and chemical (atomic proportions) data:

$$F(X_i) = \frac{1}{n} \sum_{j=1}^{n} \left(\frac{O_j - C_j(X_i)}{\sigma_j} \right)^2$$

where *n* is the number of parameters considered, O_j is the observed parameter, σ_j its standard uncertainty, X_i the variables, i.e., cation fractions at T and M sites, and $C_j(X_i)$ the corresponding quantity to O_j calculated by means of X_i parameters. Also, the constraints imposed by crystal chemistry (total charges and occupancies of T and M sites) were considered. Using a quadratic solver, the program varied the site occupancy until the calculated parameters matches the observed ones. T-O and M-O bond lengths were calculated as the linear contribution of each cation (Fe^{2+}, Fe^{3+}, and Ti^{4+}) multiplied by its empirical site bond length. The latter refined on the basis of analysis of more than 250 spinel-structural data from the literature (Lavina et al. 2002): $^{T}Fe^{2+}$-O = 2.000(1), $^{T}Fe^{3+}$-O = 1.875(2), $^{M}Fe^{2+}$-O = 2.150(2), $^{M}Fe^{3+}$-O = 2.025(1), and $^{M}Ti^{4+}$-O = 1.962(1) Å. As suggested by Lavina et al. (2002), T-O undergoes also a lengthening of 0.01 Å multiplied by $^{M}Fe^{3+}$ site populations. Lavina et al. (2002) also reported a bond length of 2.059 Å for $^{M}Fe^{2.5+}$-O, which takes into account the electron-hopping effect on the bond length. In the magnetite-ulvöspinel series, the assumption that charge hopping only involves equal numbers of $^{M}Fe^{2+}$ and $^{M}Fe^{3+}$ results in significant $^{M}Fe^{2+}$ residuals. Using this approach for octahedral Fe, results in calculated M-O lengths significant larger than the observed ones. Following Marshall and Dollase (1984), it was assumed that sub-equal amounts of Fe^{2+} and Fe^{3+} are involved in the electron hopping. Introducing an extra variable (sub-equality parameter) in the optimization procedure made electron delocalization in Fe amounts larger than twice the minimum concentration for $^{M}Fe^{2+}$ and $^{M}Fe^{3+}$ possible. Under these conditions, the calculated M-O lengths and the optimization results were substantially improved. To remove the introduced extra variable, we adopted the following final model for M-O calculations related to $^{M}Fe^{2+}$ and $^{M}Fe^{3}$. (1) All the octahedral Fe atoms participate in electron delocalization (Marshall and Dollase 1984). (2) The average valence of $<^{M}Fe^{n+}>$ is a number between 2+ and 3+ (*n*+), depending on the proportions of $^{M}Fe^{2+}$ and $^{M}Fe^{3+}$. (3) In agreement with bond-valence theory, the relation between $<^{M}Fe^{n+}>$ and its bond length $<^{M}Fe^{n+}$-O> should be described by the classic monotonic decrease of the bond valence with bond length (e.g., Shannon 1976; Brown and Altermatt 1985; Brown 2002). (4) The Mössbauer spectra of magnetite showed that an equal numbers of $^{M}Fe^{2+}$ and $^{M}Fe^{3+}$ create a net Fe valence of 2.5. As the structural refinement for magnetite resulted in a M-O = 2.060 Å, this value was applied as a model value for the $^{M}Fe^{2.5+}$-O bond length. (5) The empirical $^{M}Fe^{2+}$-O and $^{M}Fe^{3+}$-O bond lengths, the observed $^{M}Fe^{2.5+}$-O magnetite bond length, and the corresponding valence states of Fe (2+, 3+, and 2.5+, respectively), result in the relationship:

$$^{M}Fe^{n+}\text{-O} = 3.96 \times (n/6)^2 - 4.05 \times (n/6) + 3.06.$$

Note that this relationship is exclusively valid for $2 \le n \le 3$.

This model provided the best match between observed and calculated parameters in the optimization procedure (Table 3). It should be noted that the optimized site occupancies are fully consistent with the atomic proportions derived from EMPA. Table 3 presents experimental bond valences (*s*) calculated on the basis of observed bond length (*R*), by the formula $s = \exp[(R_0 - R)/B]$, where $B = 0.37$ Å and R_0 are empirical parameters (Brown and Altermatt 1985). The bond-valence analysis is consistent with the proposed cation distributions. In particular, an increase in the bond-valence sum at the M site from 2.6 to 2.9 valence units (v.u.) reflects an increase in $^{M}Ti^{4+}$ ($r^2 = 0.97$, linear regression). Concomitantly, a decrease in the bond-valence sum at the T site from 2.8 to 1.9 v.u. reflects an increase in $^{T}Fe^{2+}$ ($r^2 = 0.999$, linear regression).

Crystal chemistry

The unit-cell parameter, *u*-parameter, and T-O increase with increasing ulvöspinel component (herein expressed as the atomic proportion of $^{M}Ti^{4+}$), whereas M-O decreases comparatively little. These changes result in a sigmoid form in the crystal-chemical relationships, like the trend for *a*-parameter vs. Ti composition shown in Figure 4, which is similar to previous literature reports and attributed to non-stoichiometry (e.g., Wechsler et al. 1984; Senderov et al. 1993). In contrast to this explanation, the present study shows that the S-shaped curve is consistent with cation substitutions in fully occupied sites. In fact, crystal-chemical relationships along the entire magnetite-ulvöspinel join can be described by a cubic-model:

$$a = 8.3994 + 0.0497 \cdot [\text{Ti}] + 0.2136 \cdot [\text{Ti}]^2 - 0.1229 \cdot [\text{Ti}]^3 \ (r^2 = 0.998)$$
$$u = 0.2549 + 0.0016 \cdot [\text{Ti}] + 0.0162 \cdot [\text{Ti}]^2 - 0.0083 \cdot [\text{Ti}]^3 \ (r^2 = 0.995)$$

where [Ti] is the titanium concentration (apfu).

To a first approximation, the Akimoto model $^{T}(Fe^{3+}_{1-X}Fe^{2+}_{X})$ $^{M}(Fe^{2+}Fe^{3+}_{1-X}Ti_X)O_4$ describes the cation substitutions in the present

TABLE 3. Cation distribution, bond valence, and residual parameters relative to the optimization procedure

Crystal	Mgt100	FeTi10C	FeTi50B	FeTi10Ai	FeTi10Ao	FeTi20A	FeTi30A	FeTi50Bd	FeTi50C
T site									
Fe^{2+} (apfu)	0.000	0.067	0.076	0.103	0.162	0.267	0.385	0.579	0.640
Fe^{3+}	1.000	0.933	0.924	0.897	0.838	0.733	0.615	0.421	0.360
Total	1.000	1.000	1.000	1.000	1.000	1.000	1.000	1.000	1.000
M site									
Fe^{2+} (apfu)	1.000	1.029	1.023	1.083	1.080	1.086	1.077	1.007	1.004
Fe^{3+}	1.000	0.875	0.879	0.731	0.678	0.530	0.461	0.380	0.352
Ti^{4+}	0.000	0.096	0.098	0.186	0.242	0.354	0.462	0.585	0.644
Al	0	0	0	0	0	0.030	0	0.028	0
Total	2.000	2.000	2.000	2.000	2.000	2.000	2.000	2.000	2.000
T-BVS (v.u.)	2.83	2.78	2.76	2.75	2.68	2.59	2.47	2.29	2.23
M-BVS	2.57	2.58	2.58	2.58	2.60	2.62	2.66	2.73	2.74
ΔT-O (Å)	0.002(2)	0.000(2)	0.001(2)	0.000(2)	0.000(2)	0.001(2)	0.000(2)	0.000(2)	0.000(2)
ΔM-O (Å)	0.000(2)	0.001(2)	0.001(2)	0.001(2)	0.000(2)	0.000(2)	0.000(1)	0.000(1)	0.001(1)
Δ*a* (Å)	0.003(6)	0.002(6)	0.004(5)	0.002(5)	0.001(6)	0.003(5)	0.000(5)	0.000(5)	0.003(5)
Δ*u*	0.0001(2)	0.0000(2)	0.0000(1)	0.0000(2)	0.0000(2)	0.0000(2)	0.0000(1)	0.0000(1)	0.0000(1)

Crystal	FeTi40A	FeTi60A	FeTi70A	FeTi80Ac	FeTi80Af	FeTib3	FeTib2	FeTib4	FeTib1c	FeTib1b
T site										
Fe^{2+} (apfu)	0.700	0.755	0.813	0.789	0.779	0.869	0.936	1.000	1.000	1.000
Fe^{3+}	0.300	0.245	0.187	0.211	0.221	0.131	0.064	0.000	0.000	0.000
Total	1.000	1.000	1.000	1.000	1.000	1.000	1.000	1.000	1.000	1.000
M site										
Fe^{2+} (apfu)	1.012	0.936	0.939	0.962	0.976	0.931	0.909	0.908	0.930	0.945
Fe^{3+}	0.275	0.374	0.309	0.287	0.268	0.268	0.246	0.184	0.140	0.110
Ti^{4+}	0.713	0.690	0.752	0.751	0.756	0.800	0.845	0.908	0.930	0.945
Al	0	0	0	0	0	0	0	0	0	0
Total	2.000	2.000	2.000	2.000	2.000	2.000	2.000	2.000	2.000	2.000
T-BVS (v.u.)	2.16	2.12	2.08	2.10	2.11	2.03	1.98	1.93	1.92	1.92
M-BVS	2.77	2.79	2.81	2.79	2.78	2.83	2.85	2.88	2.88	2.88
ΔT-O (Å)	0.001(2)	0.002(2)	0.001(3)	0.001(2)	0.001(2)	0.002(2)	0.002(2)	0.002(2)	0.005(2)	0.005(2)
ΔM-O (Å)	0.000(1)	0.002(2)	0.002(2)	0.002(1)	0.001(1)	0.001(1)	0.002(1)	0.000(1)	0.002(1)	0.003(1)
Δ*a* (Å)	0.001(5)	0.009(6)	0.006(6)	0.006(5)	0.006(5)	0.007(5)	0.009(4)	0.003(5)	0.001(4)	0.002(5)
Δ*u*	0.0000(2)	0.0000(2)	0.0000(2)	0.0000(1)	0.0000(2)	0.0000(1)	0.0000(1)	0.0001(2)	0.0003(2)	0.0004(2)

Notes: In parentheses the uncertainty parameter (estimated by error propagation) in Δ at the 68% confidence level (±1σ). The uncertainty for ΔT-O and ΔM-O includes uncertainty in observed and empirical bond length; uncertainty in Δ*a* and Δ*u* includes the uncertainties in calculated bond lengths and that in observed *a*- and *u*-parameter (respectively). ^{T}Al-O = 1.774(1) and ^{M}Al-O = 1.908(1) Å were used during the optimization procedure in the samples with Al. Δ = absolute deviation between observed and calculated parameter. Note that ΔFe^{2+} and ΔFe^{3+} values are <0.003 apfu. T- and M-BVS = experimental bond valence sums at the T and M sites.

titanomagnetites. However, minor deviations occur from it as a consequence of the following electron exchange reaction:

$$^{T}Fe^{2+} + {}^{M}Fe^{3+} = {}^{T}Fe^{3+} + {}^{M}Fe^{2+}. \quad (4)$$

This is an internal reaction that involves the transfer of an electron between the T and M sites, causing $^{M}Fe^{2+} \neq 1$, $^{T}Fe^{2+}/Ti \neq 1$, and non-linear relations between Ti and Fe^{3+} (Fig. 5). However, these deviations are neither consistent with the models of Néel-Chevallier nor O'Reilly-Banerjee. The obtained S-shaped trends may be related to a directional change in the internal reaction 4, summarized as

$$^{T}e^{-} \rightarrow {}^{M}e^{-}, \text{ for Ti} < 0.7 \text{ apfu} \quad (5)$$
$$^{T}e^{-} \leftarrow {}^{M}e^{-}, \text{ for Ti} > 0.7 \text{ apfu}. \quad (6)$$

With respect to the Akimoto model, the electron exchange reaction 5 yields more Fe^{2+} at the M site, while reaction 6 results in less Fe^{2+} at the M site. Figure 6 demonstrates clearly the observed deviation from the expected linearity of the Akimoto model by the sigmoid relationship between the T-O length and Ti^{4+} content. As the structure variations are mainly driven by T-O, the S-shaped trends are also evident for the *a* and *u* relationships. In general, variations in structural parameters over the whole compositional range can be split into two contributions: a linear variation due to the $^{T}Fe^{3+} + {}^{M}Fe^{3+} = {}^{T}Fe^{2+} + {}^{M}Ti^{4+}$ chemical substitution, and non-linear variations caused by the internal electron exchange reaction 4.

Site occupancy preference

To estimate the site preference of Fe^{2+} and Fe^{3+}, the fractional parameters $Q Fe^{2+} = {}^{T}Fe^{2+}/\Sigma Fe^{2+}$ and $Q Fe^{3+} = {}^{T}Fe^{3+}/\Sigma Fe^{3+}$ were calculated. As the ratio between occupied T and M sites in the structure is 1:2, values of $Q < 1/3$ indicates a preference for the M site, whereas $Q > 1/3$ indicates T site preference.

Figure 7 illustrates the trends of $Q Fe^{2+}$ and $Q Fe^{3+}$ vs. Ti. The $Q Fe^{3+}$ trend reveals that Fe^{3+} has a preference for the T site at approximately Ti < 0.8 apfu, and for the M site at higher Ti content. Note, that according to the Akimoto model, Fe^{3+} should always prefer the T site. The $Q Fe^{2+}$ value directly increases with increasing Ti^{4+}. As a consequence, the Fe^{2+} site preference changes from M to T as the composition becomes richer in ulvöspinel component. It should be noted that the T site is fully occupied by Fe^{2+} for $Ti^{4+} > 0.9$ apfu. The deviation from the

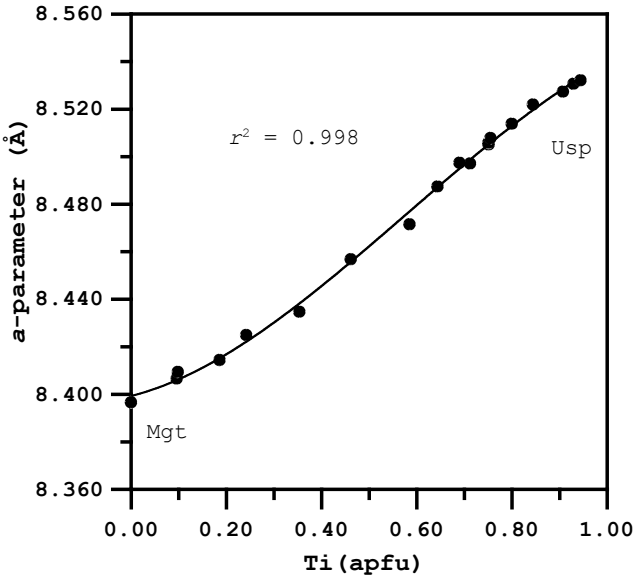

FIGURE 4. The variation of the *a*-parameter vs. ulvöspinel content (expressed as Ti pfu) can be described by an S-shaped curve (cubic regression). In contrast to the literature, which explains this variation by non-stoichiometry, the present titanomagnetites are stoichiometric. Symbol dimensions are proportional to 2σ.

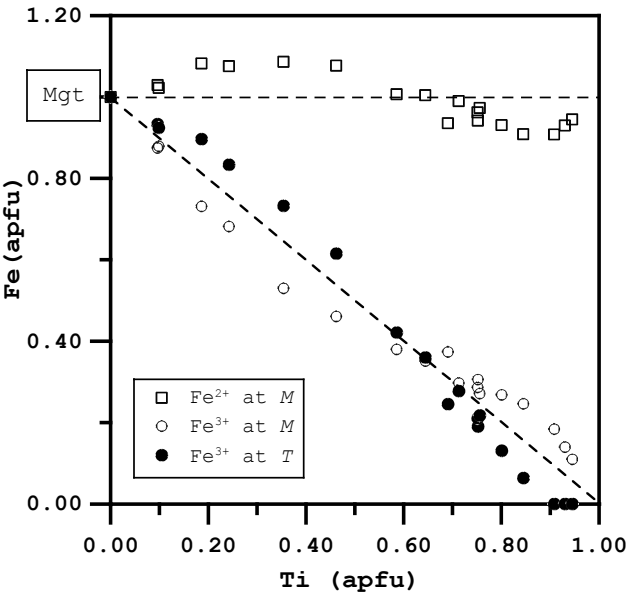

FIGURE 5. Variation of the Fe content at the T and M sites with Ti. Note the S-shaped form of the trends and their deviations from the Akimoto model (dashed lines). Symbol dimensions are proportional to 2σ.

Akimoto model appears also in this case to be a consequence of the internal reaction 4. Therefore, it is important to explore the reasons for this reaction.

Typically, the preference of Fe^{3+} for the T site is explained by its tendency to form sp^3 bonds (Goodenough and Loeb 1955). This explanation is in agreement with T-O being smaller than M-O in the present titanomagnetites. This, in turn, implies that small cations are accommodated at the T sites. Consequently, to reduce the size of the tetrahedron by creating more $^{T}Fe^{3+}$, an electron may be transferred from T to M. Simultaneously, as a

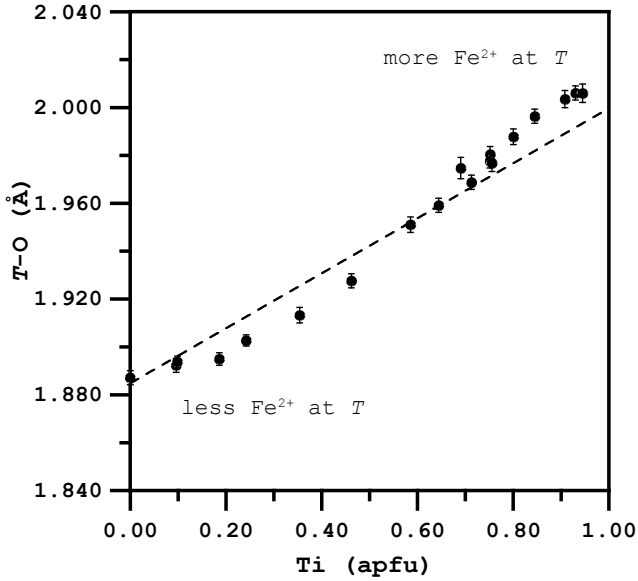

FIGURE 6. Relationship between T-O and Ti, in comparison with the linear variation expected from the Akimoto model (dashed line calculated using empirical bond lengths, see text). $^{T}Fe^{2+}$ contents less than expected yield negative T-O deviations and a region of concave-upward curvature. $^{T}Fe^{2+}$ contents greater than expected yield positive T-O deviations and a region of convex-upward curvature. As a result, the fully occupied site can describe an S-shaped curve. Symbol dimensions and error bars, where shown, are proportional to 2σ.

charge-compensation effect, $^{M}Fe^{3+}$ is reduced to Fe^{2+}, thus yielding $^{M}Fe^{2+} > 1$ apfu. In this way, observed deviations from the Akimoto model for Ti < 0.7 apfu are explained. As the Ti^{4+}-Ti^{4+} repulsion between adjacent octahedra is strong and the probability for ^{M}Ti-^{M}Ti pairs is very high for Ti > 0.7 apfu, an electron may move from M to T creating more $^{T}Fe^{2+}$ at increasing T-O bond lengths. In this way, $^{M}O\text{-}O_{shared}$ can decrease more effectively (as suggested by the non-linear relation in Fig. 3), thus providing a shielding effect that reduces Ti^{4+}-Ti^{4+} repulsion, and thus moves the structural state toward a free energy minimum. As a charge-compensation effect, $^{M}Fe^{2+}$ is oxidized to $^{M}Fe^{3+}$. This effect induces Fe^{2+}/Fe^{3+} electron delocalization at the M sites, which is expected to stabilize the structure (Waychunas 1991).

Structural stability

In a previous section we have shown that bond-valence sums, calculated according to the formula of Brown and Altermatt (1985), provide a useful tool for evaluating the consistency of average site valency in relation to cation distribution. In polyhedra having bonds of equal length, bond-valence values should match the bond-strength values estimated by Pauling's electrostatic valence principle. If this match is not obtained, several causes might be invoked (e.g., Brown 2002), such as an artifact of the bond-valence parameters used or an indication of internal strain in the bonds.

As the incorporation of Ti^{4+} at octahedra in spinels leads to an increase in the M-M repulsive potential as well as to a pronounced M-site cation-size/valence mismatch, i.e., Ti^{4+} and Fe^{2+} on adjacent M site. This cationic arrangement may introduce strain in the spinel structure. In the following, we consider the

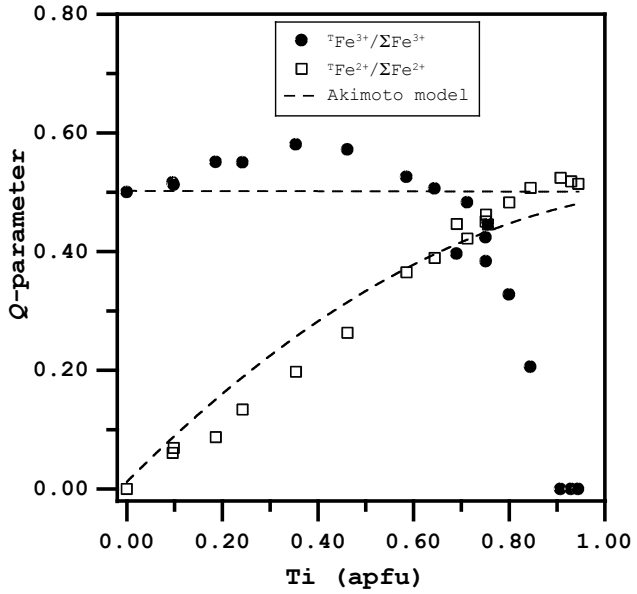

FIGURE 7. Plot of the site preference (Q) of Fe vs. ulvöspinel content (Ti pfu) showing the Fe^{2+} and Fe^{3+} partitioning with respect to the Akimoto model. Note the observed S-shaped curves crossing the model at Ti ≈ 0.7 apfu.

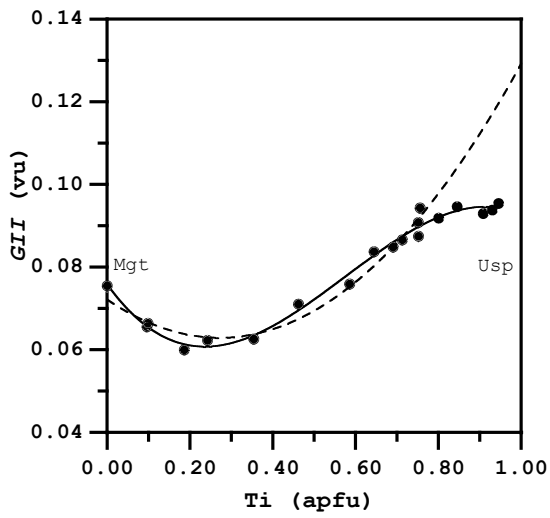

FIGURE 8. Relationship between the global instability index (*GII*) and the ulvöspinel content (Ti pfu). The solid line is a cubic regression ($r^2 = 0.98$) based on all samples. The dashed line is a quadratic regression ($r^2 = 0.96$) obtained using samples with Ti < 0.75 apfu.

internal strain by applying the bond-valence model (e.g., Brown 2002) to the spinel structure.

A criterion to clarify important structural features such as the presence and extent of strain is stated in the equal-valence rule of the bond-valence model—there is a tendency for experimental bond valences around each atom to approach formal valence. Large mismatches between them are indicative of strained bonds that may lead to structural instabilities. The global instability index (*GII*, Brown 2002), i.e., the root mean square deviation of the bond valence sums from the formal valence averaged over all atoms, measures the extent to which the valence sum rule is violated. Any increase in *GII* to values >0.05 v.u. indicates progressive instability in the structure. In the magnetite-ulvöspinel series, *GII* values higher than 0.06 v.u. indicate that the structure has strained bonds ascribable to steric effects (Brown 2002). *GII* is relatively large for magnetite, and with increasing Ti up to ca. 0.7 apfu it follows a concave curve (Fig. 8). This trend may be explained by the electron transfer from T to M to relax the bonds and to minimize the strain:

$$^{T}Fe^{2+} + {}^{M}Fe^{3+} \rightarrow {}^{T}Fe^{3+} + {}^{M}Fe^{2+}. \quad (7)$$

Nonetheless, reaction 7 leads to a significant increase in strain for Ti > 0.7 apfu, ultimately leading to a predicted *GII* value ≈ 0.13 v.u. for the ulvöspinel end-member (Fig. 8). The observed relaxation, in the Ti-rich part of the solid solution, can be explained by transfer of an electron in a direction opposite to reaction 7, i.e., from M to T:

$$^{T}Fe^{2+} + {}^{M}Fe^{3+} \leftarrow {}^{T}Fe^{3+} + {}^{M}Fe^{2+}. \quad (8)$$

Reaction 8 explains both the observed sharp break of the strain in the region where *GII* ≈ 0.09 v.u. and Ti > 0.7 apfu and the relaxation at the Ti-rich side, the convex curve in Figure 8. This is, in fact, also the part where Fe^{2+}- and Fe^{3+}-site preference trends cross as a consequence of direction changes in the electron exchange reaction to reduce the M-site cation-size/valence mismatch.

In conclusion, non-linear variations in the crystal-chemical relationships of the magnetite-ulvöspinel series may be explained by an electron exchange reaction between Fe cations in fully occupied sites. This reaction seems to be consistent with a relaxation of the bonds to minimize the internal strain at retained spinel space group symmetry.

ACKNOWLEDGMENTS

Financial support from the Swedish Research Council through the ESF-program EuroMinSci is gratefully acknowledged. H. Harryson, Uppsala University, is thanked for careful microprobe analytical work. We thank S. Lucchesi for making the single-crystal XRD-facility at the University of Rome "La Sapienza" accessible. Careful and helpful reviews by A. Della Giusta and G.B. Andreozzi are greatly appreciated.

REFERENCES CITED

Akimoto, S. (1954) Thermomagnetic study of ferromagnetic minerals contained in igneous rocks. Journal of Geomagnetism and Geoelectricity, 6, 1–14.

Bleil, U. (1971) Cation distribution in titanomagnetites. Zeitschrift für Geophysik, 37, 305–319.

——— (1976) An experimental study of the titanomagnetite solid solution series. Pure and Applied Geophysics, 114, 165–175.

Bosi, F., Hålenius, U., Andreozzi, G.B., Skogby, H., and Lucchesi, S. (2007) Structural refinement and crystal chemistry of Mn-doped spinel: A case for tetrahedrally coordinated Mn^{3+} in an oxygen-based structure. American Mineralogist, 92, 27–33.

Bosi, F., Hålenius, U., and Skogby, H. (2008) Stoichiometry of synthetic ulvöspinel single crystals. American Mineralogist, 93, 1312–1316.

Brown, I.D. (2002) The Chemical Bond in Inorganic Chemistry: the Bond Valence Model, 288 p. International Union of Crystallography Monographs on Crystallography No. 12, Oxford University Press, New York.

Brown, I.D. and Altermatt, D. (1985) Bond-valence parameters obtained from a systematic analysis of the Inorganic Crystal Structure Database. Acta Crystallographica, B41, 244–247.

Chevallier, R., Bolfa, J., and Mathieu, S. (1955) Titanomagnetites et ilmenites ferromagnetiques. (I) Etude optique, radiocristallographique, chimique. Bulletin de la Societe Francaise de Mineralogie et de Cristallographie, 78, 307–346.

Fujino, K. (1974) Cation distribution and local variation of site symmetry in solid solution series, Fe_3O_4-Fe_2TiO_4. Mineralogical Journal, 7, 472–488.

Goodenough, J.B. and Loeb, A.L. (1955) Theory of ionic ordering, crystal dis-

tortion, and magnetic exchange due to covalent forces in spinels. Physical Review, 98, 391–408.
Häggström, L., Annersten, H., Ericsson, T., Wäppling, R., Karner, W., and Bjarman, S. (1978) Magnetic dipolar and electric quadrupolar effects on Mössbauer-spectra of magnetite above Verwey transition. Hyperfine Interactions, 5, 201–214.
Jernberg, P. and Sundqvist, T. (1983) A versatile Mössbauer analysis program. Uppsala University, Institute of Physics (UUIP-1090).
Lavina, B., Salviulo, G., and Della Giusta, A. (2002) Cation distribution and structure modeling of spinel solid solutions. Physics and Chemistry of Minerals, 29, 10–18.
Marshall, C.P. and Dollase, W.A. (1984) Cation arrangement in iron-zinc-chromium spinel oxides. American Mineralogist, 69, 928–936.
Néel, L. (1955) Some theoretical aspects of rock magnetism. Advances in Physics, 4, 191–243.
North, A.C.T., Phillips, D.C., and Mathews, F.S. (1968) A semi-empirical method of absorption correction. Acta Crystallographica, A24, 351–359.
O'Donovan, J.B. and O'Reilly, W. (1980) The temperature dependent cation distribution in titanomagnetites: An experimental test. Physics and Chemistry of Minerals, 5, 235–243.
O'Reilly, W. and Banerjee, S.K. (1965) Cation distribution in titanomagnetites $(1–x)Fe_3O_4$-xFe_2TiO_4. Physics Letters, 17, 237–238.
Pouchou, J.L. and Pichoir, F. (1991) Quantitative analysis of homogeneous or stratified microvolumes applying the model "PAP." In K.F.J. Heinrich and D.E. Newbury, Eds., Electron Probe Quantitation, p. 31–75. Plenum, New York.
Price, G.D. (1981) Subsolidus phase relations in the titanomagnetite solid solution series. American Mineralogist, 66, 751–758.
Sedler, I.K., Feenstra A., and Peters, T. (1994) An X-ray powder diffraction study of synthetic $(Fe,Mn)_2TiO_4$ spinel. European Journal of Mineralogy, 6, 873–885.
Senderov, E., Dogan, U., and Navrotsky, A. (1993) Nonstoichiometry of magnetite-ulvöspinel solid solutions quenched from 1300 °C. American Mineralogist, 78, 565–573.
Shannon, R.D. (1976) Revised effective ionic radii and systematic studies of interatomic distances in halides and chalcogenides. Acta Crystallographica, A32, 751–767.
Sheldrick, G.M. (1997) SHELXL-97-1. Program for crystal structure determination. University of Göttingen, Germany.
Stephenson, A. (1969) The temperature dependent cation distribution in titanomagnetites. Geophysical Journal of the Royal Astronomical Society, 18, 199–210.
Stout, M.Z. and Bayliss, P. (1980) Crystal structure of two ferrian ulvöspinels from British Columbia. Canadian Mineralogist, 18, 339–341.
Waychunas, G.A. (1991) Crystal chemistry of oxides and oxyhydroxides. In D.H. Lindsley, Ed., Oxide Minerals: Petrologic and Magnetic Significance, 25, p. 11–68. Reviews in Mineralogy, Mineralogical Society of America, Chantilly, Virginia.
Wechsler, B.A., Lindsley, D.H., and Prewitt, C.T. (1984) Crystal structure and cation distribution in titanomagnetites $(Fe_{3-x}Ti_xO_4)$. American Mineralogist, 69, 754–770.
Wood, B.J. and Virgo, D. (1989) Upper mantle oxidation state: Ferric iron contents of lherzolite spinels by ^{57}Fe Mössbauer spectroscopy and resultant oxygen fugacity. Geochimica et Cosmochimica Acta, 53, 1277–1291.

Manuscript received April 22, 2008
Manuscript accepted July 9, 2008
Manuscript handled by Joshua Feinberg